

# Alignment of Galaxies and Clusters

Yasuhiro Hashimoto<sup>1,3\*</sup> J. Patrick Henry<sup>1,2</sup> and Hans Boehringer<sup>1</sup>

<sup>1</sup>*Max-Planck-Institut für extraterrestrische Physik, Giessenbachstrasse D-85748 Garching, Germany*

<sup>2</sup>*Institute for Astronomy, University of Hawaii, 2680 Woodlawn Drive, Honolulu, Hawaii 96822, USA*

<sup>3</sup>*South African Astronomical Observatory, Observatory 7935, South Africa*

Accepted xx. Received xx

## ABSTRACT

We investigated the influence of environment on cluster galaxies by examining the alignment of the brightest cluster galaxy (BCG) position angle with respect to the host cluster X-ray position angle. The cluster position angles were measured using high spatial resolution X-ray data taken from the Chandra ACIS archive, that significantly improved the determination of the cluster shape compared to the conventional method of using optical images. Meanwhile, those of the BCGs were measured using homogeneous dataset composed of high spatial resolution optical images taken with Suprime-Cam mounted on Subaru 8m telescope.

We found a strong indication of an alignment between the cluster X-ray emission and optical light from BCGs, while we see no clear direct correlation between the degree of ellipticity of X-ray and optical BCG morphologies, despite the apparent alignment of two elliptical structures. We have also investigated possible dependence of the position angle alignment on the X-ray morphology of the clusters, and no clear trends are found. The fact that no trends are evident regarding frequency or degree of the alignment with respect to X-ray morphology may be consistent with an interpretation as a lack of dependence on the dynamical status of clusters.

**Key words:** Galaxies: clusters: general – X-rays: galaxies: clusters – Galaxies: evolution

## 1 INTRODUCTION

It is well established that the major axes of galaxy clusters tend to point toward their nearest neighbour (e.g. Binggeli 1982; Flin 1987; Rhee & Katgert 1987; Plionis 1994; West et al. 1995; Plionis & Basilakos 2002; Chambers et al. 2000, 2002, Hashimoto et al. 2007a).

Another alignment effect is that between the orientation of the brightest cluster galaxy (BCG), or cD galaxy, and that of their parent cluster (e.g. Sastry 1968; Dressler 1978; Carter & Metcalfe 1980; Binggeli 1982; Struble 1990; Plionis et al. 2003). Similar alignment is also reported for poor groups of galaxies (Fuller et al. 1999). Numerical work (e.g. West et al. 1991; van Haarlem & van de Weygaert 1993; West 1994; Onuora & Thomas 2000; Splinter et al. 1997; Faltenbacher et al. 2005) show that substructure-cluster alignments can occur naturally in hierarchical clustering models of structure formation such as the cold dark matter model.

Unfortunately, all of these previous galaxy-cluster alignment studies are using optically-determined cluster

position angles, most of them are based on the Palomar Observatory Sky Survey (POSS). Despite the importance of these optical investigations, individual galaxies may not be the best tracers of the shape of a cluster. Problems can arise from foreground/background contamination, as well as the fact that galaxies contribute discreteness noise. However, it is believed that the X-ray emitting gas within a cluster traces its gravitational potential (Sarazin 1986). X-ray morphology may then be one of the best observable phenomenon for determining the cluster shape and orientation. Indeed, there are several X-ray studies for cluster vs. neighbour-cluster alignment (e.g. Ulmer, McMillan & Kowalski 1989; Chambers, Melott & Miller 2000, 2002, Hashimoto et al. 2007a), but there are few galaxy-cluster alignment studies using X-ray morphology, except for Porter, Schneider & Hoessel (1991) and Rhee & Latour (1991), where they investigated the BCG-cluster alignment using low spatial resolution X-ray data, as well as traditional cluster shape parameter from apparent galaxy distribution, and reported a significant alignment. Unfortunately, previous X-ray studies are mostly based on *Einstein* data. These data are important, but the exposure depths are small and the spatial resolution is rather low compared

\* Contacting email: hashimot@sao.ac.za

to recently available X-ray data. The low spatial resolution may not significantly affect relatively robust measures such as position angle in a direct way, but it will critically hinder the accurate removal of contaminating point sources and the accurate determination of cluster center, and that may significantly affect the estimate of cluster X-ray morphology including the position angle. Hence, a new investigation using deeper X-ray data with much higher spatial resolution is needed.

Here we report a new investigation of galaxy alignment with respect to its parent cluster, using the cluster position angle and ellipticity determined by high spatial resolution X-ray data taken from the Chandra ACIS archive. Meanwhile, position angle and ellipticity of BCGs are determined from optical images taken with Subaru 8m telescope. This paper is organized as follows. In Sec. 2, we describe our main sample and X-ray measures, in Sec. 3, details of our optical data are described. Sec. 4 summarizes our results. Throughout the paper, we use  $H_o = 70 \text{ km s}^{-1} \text{ Mpc}^{-1}$ ,  $\Omega_m = 0.3$ , and  $\Omega_\Lambda = 0.7$ , unless otherwise stated.

## 2 THE X-RAY SAMPLE, X-RAY DATA PREPARATION, AND X-RAY MEASURES

Here we briefly summarize our main X-ray sample, X-ray data preparation, and X-ray measures. More detailed descriptions can be found in Hashimoto et al. (2007b).

Almost all clusters are selected from flux-limited X-ray surveys, and X-ray data are taken from the Chandra ACIS archive. A lower limit of  $z = 0.05$  or  $0.1$  is placed on the redshift to ensure that a cluster is observed with sufficient field-of-view with ACIS-I or ACIS-S, respectively. The majority of our sample comes from the *ROSAT* Brightest Cluster Sample (BCS; Ebeling et al. 1998) and the Extended *ROSAT* Brightest Cluster Sample (EBCS; Ebeling et al. 2000). When combined with EBCS, the BCS clusters represent one of the largest and most complete X-ray selected cluster samples, which is currently the most frequently observed by *Chandra*. To extend our sample to higher redshifts, additional high- $z$  clusters are selected from various deep surveys; 10 of these clusters are selected from the *ROSAT* Deep Cluster Survey (RDCS; Rosati et al. 1998), 10 from the *Einstein* Extended Medium Sensitivity Survey (EMSS; Gioia et al. 1990; Henry et al. 1992), 14 from the 160 Square Degrees *ROSAT* Survey (Vikhlinin et al. 1998), 2 from the Wide Angle *ROSAT* Pointed Survey (WARPS; Perlman et al. 2002), and 1 from the North Ecliptic Pole survey (NEP; Henry et al. 2006), RXJ1054 was discovered by Hasinger et al. (1998), RXJ1347 was discovered in the *ROSAT* All Sky Survey (Schindler et al. 1995), and 3C295 has been mapped with *Einstein* Henry & Henriksen (1986).

The resulting sample contains 120 clusters. At the final stage of our data processing, to employ our full analysis, we further applied a selection based on the total counts of cluster emission, eliminating clusters with very low signal-to-noise ratio. Clusters whose center is too close to the edge of the ACIS CCD are also removed. The resulting final sample contains 101 clusters with redshifts between 0.05 - 1.26 (median  $z = 0.226$ ), and bolometric luminosity between  $1.0 \times 10^{44} - 1.2 \times 10^{46} \text{ erg s}^{-1}$  (median  $8.56 \times 10^{44} \text{ erg s}^{-1}$ ). We reprocessed the level=1 event file retrieved from the archive.

The data were filtered to include only the standard event grades 0,2,3,4,6 and status 0, then multiple pointings were merged, if any. We eliminated time intervals of high background count rate by performing a  $3\sigma$  clipping of the background level. We corrected the images for exposure variations across the field of view, detector response and telescope vignetting.

We detected point sources using the CIAO routine `celldetect` with a signal-to-noise threshold for source detection of three. We removed point sources, except for those at the center of the cluster which was mostly the peak of the surface brightness distribution rather than a real point source. The images were then smoothed with Gaussian  $\sigma=5''$ . We decided to use isophotal contours to characterize an object region, instead of a conventional circular aperture, because we did not want to introduce any bias in the shape of an object. To define constant metric scale to all clusters, we adjusted an extracting threshold in such a way that the square root of the detected object area times a constant was 0.5 Mpc, i.e.  $\text{const} \sqrt{\text{area}} = 0.5 \text{ Mpc}$ . We chose  $\text{const} = 1.5$ , because the isophotal limit of a detected object was best represented by this value.

The morphology of cluster X-ray emission is then characterized objectively by the position angle, as well as the ellipticity and the asymmetry. The position angle is defined by the orientation of the major axis measured east from north. Ellipticity is simply defined by the ratio of semi-major (A) and semi-minor axis (B) lengths as:

$$Elli = 1 - B/A \quad (1)$$

where A and B are defined by the maximum and minimum spatial *rms* of the object profile along any direction and computed from the centered-second moments by the formula:

$$A^2 = \frac{\overline{x^2} + \overline{y^2}}{2} + \sqrt{\left(\frac{\overline{x^2} - \overline{y^2}}{2}\right)^2 + \overline{xy}^2} \quad (2)$$

$$B^2 = \frac{\overline{x^2} + \overline{y^2}}{2} - \sqrt{\left(\frac{\overline{x^2} - \overline{y^2}}{2}\right)^2 + \overline{xy}^2} \quad (3)$$

The asymmetry is measured by first rotating a cluster image by 180 degrees around the object center, then subtracting the rotated image from the original unrotated one. The residual signals above zero are summed and then normalized. Please see Hashimoto et al. 2007b for more detailed definitions of morphological measures.

## 3 OPTICAL DATA

To determine the position angle and the ellipticity of BCGs, we used optical broad band images taken with Supreme-Cam (Miyazaki et al. 1998) on the Subaru telescope. The data were retrieved from Subaru-Mitaka-Okayama-Kiso Archive (SMOKA). Reduction software developed by Yagi et al. (2002) was used for flat-fielding, instrumental distortion correction, differential refraction, sky subtraction, and stacking. The camera covers a  $34' \times 27'$  field of view with a pixel scale of  $0''.202$ . The photometry is calibrated to Vega system using Landolt standards (Landolt 1992). We refine the original astrometry written as WCS keyword in the distributed

archival data using using USNO-A2 catalog with positional uncertainties less than  $\sim 0.2$  arcsec. The data were taken under various seeing conditions, and we used only images with less than  $\sim 1''.2$  seeing. The optical data retrieved from SMOKA contains 30 clusters with redshifts between 0.08 - 0.9,

Some clusters have observed through many wavebands, and that allowed us to investigate the possible variations of our measures caused by waveband shifts. We have decided to rely primarily on the R band images for this alignment study, because we found that the effect of waveband shift is negligible.

The position angle and ellipticity of BCGs are measured exactly the same way as the X-ray cluster emission, namely, the position angle is defined by the orientation of the major axis measured east from north, and the ellipticity is defined by the ratio of semi-major and semi-minor axis. Please see Hashimoto et al. 2007b (see also Hashimoto et al. 1998) for further details. As a precaution, we investigate the effect of superposed small galaxies sometimes lying on top of the extended structure of some BCGs, and we found that these superposed small galaxies have little effect on our robust measures such as, position angle and ellipticity.

## 4 RESULTS

### 4.1 Systematics

One of the haunting, yet unfortunately often lightly treated, problem of any study comparing complex morphological characteristics of astronomical objects is the possible systematics introduced by various data quality, exposure times and object redshifts. Depending on the sensitivity of measures of characteristics, some susceptible measures may be seriously affected by these systematics, producing the misleading results.

Unfortunately, investigating the systematics on the complex characteristics is not an easy task. To investigate the systematic effect of, for example, various exposure times, one of the standard approaches is to simulate an image with a given exposure time by using an exposure-time-scaled and noise-added model image. Unfortunately, we need to approximate the various characteristics of a model to the complicated characteristics of a real object, (and those characteristics are often what we want to investigate) and this is an almost impossible task.

Meanwhile, if we use the real data, instead of the model, we will not have this problem. We can simulate lower signal-to-noise data caused by a shorter integration time by scaling the real data by the exposure time, and adding Poisson noise taking each pixel value as the mean for a Poisson distribution. However, this simple rescaling and adding-noise process will produce an image containing an excessive amount of Poisson noise for a given exposure time, thus lead us to underestimate the data quality. This inaccurate estimate of noise is caused by the intrinsic noise already presented in the initial real data. The intrinsic noise is difficult to be removed without sacrificing the fine spatial details of the object.

Similarly, to investigate the effect of dimming and smaller angular size caused by higher redshifts, in addition to the rest waveband shift effect, simple rescaling and rebin-

ning of the real data will not work, because these manipulations will again produce the incorrect amount of noise.

Further difficulty associated with simulation using the real data comes from the fact that exposure and redshift effects are often coupled, because, in the real observation, low redshift objects are usually observed with shorter exposures than high redshift objects. This coupling further poses a serious problem, because simple standard method of simulating an observation with ‘decreased’ exposure time will force high redshift data to get degraded, which greatly reduces signal-to-noise ratio of already low quality high redshift data.

To circumvent all of these challenging problems, we developed a very useful simulating technique employing a series of ‘adaptive scalings’ accompanied by a noise adding process applied to the real images. This technique allows us to simulated an image of desired fiducial exposure time and redshift with correct signal-to-noise ratio without using a tricky artificial model image, thus we can easily investigate the effect of various image quality and/or easily change the real data to common fiducial exposure and redshift for easy comparison. Moreover, the technique can provide us with a powerful tool for conducting evolutionary studies, enabling us to compare the local objects to the high redshift objects without degrading photon-expensive high redshift data of low signal-to-noise ratio at all. This method is originally developed for the comparison of X-ray image data, but can be used for almost all kind of imaging data, including optical and NIR images.

Here we briefly describe the method. Please see Hashimoto et al. 2007b for further details. To simulate data with integration  $t=t_1$ , an original unsmoothed image (including the background) taken with original integration time  $t_0$  was at first rescaled by a factor  $R_0/(1-R_0)$ , instead of simple  $R_0$ , where  $R_0=t_1/t_0$ ,  $t_0>t_1$ . That is, an intermediate scaled image  $I_1$  was created from the original unsmoothed image  $I_0$  by:

$$I_1 = I_0 \frac{R_0}{(1 - R_0)}. \quad (4)$$

Poisson noise was then added to this rescaled image by taking each pixel value as the mean for a Poisson distribution and then randomly selecting a new pixel value from that distribution. This image was then rescaled again by a factor  $(1-R_0)$  to produce an image whose *signal* is scaled by  $R_0$  relative to the original image, but its *noise* is approximately scaled by  $\sqrt{R_0}$ , assuming that the intrinsic noise initially present in the real data is Poissonian.

Similarly, to simulate the dimming effect by the redshift, an intermediate scaled image  $I_1$  is created from the background subtracted image  $I_0$  by a pixel-to-pixel manipulation:

$$I_1(x, y) = \frac{I_0(x, y)^2 R_1^2}{[I_0(x, y) R_1 + B - R_1^2 (I_0(x, y) + B)]} \quad (5)$$

where

$$R_1 = [(1 + z_0)/(1 + z_1)]^4 \quad (6)$$

where  $z_0$  and  $z_1$  are the original redshift and the new redshift of the object, respectively, and  $B$  is the background.

Finally, to simulate the angular-size change due to the redshift difference between  $z_0$  and  $z_1$ , the original image will

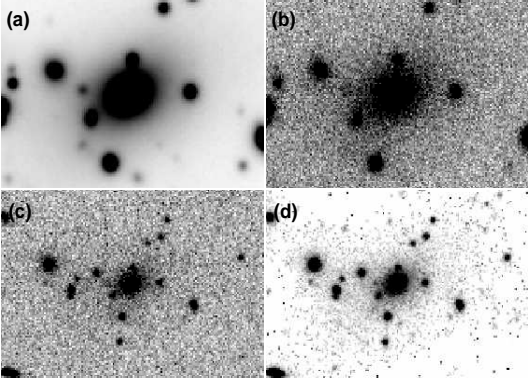


**Figure 1.** Simulating an image with desired exposure time and redshift using the real data: Even simulating an image with prolonged exposure time is possible with our adaptive scaling method. Here, optical R band images, taken with Subaru Suprime-Cam, of the BCG at the center of an example cluster (Abell 2219) are shown. Images with original and modified exposure time and redshift are presented with north is up and east is left. (a) Original image:  $\text{exptime}(t)=240\text{s}$ , and  $\text{redshift}(z)=0.228$ , (b) Simulated shorter exposure image with  $t=10\text{s}$  (c) Simulated high- $z$  image with  $z=0.9$ ,  $t=240\text{s}$  (d) Simulated prolonged exposure at high- $z$  with  $t=1092\text{s}$ ,  $z=0.9$ .

be rebinned by a factor  $R_2$ , then intermediate scaled image will be created by rescaling the rebinned image by a factor  $1/(R_2^2-1)$ , before the addition of the Poisson noise. For the simulation with ‘increased’ exposure time, this factor can be changed to  $R_3/(R_2^2-R_3)$  where  $R_3 = t_2/t_0$ ,  $t_2 > t_0$ , where  $t_2$  is the increased exposure time, and  $t_0$  is the original integration time, and  $(R_2^2 - R_3) > 0$ . The maximum length of integration time we can ‘increase’ ( $t_{2max}$ ) is naturally limited by the original exposure time and how much we increase the redshift for the redshift-effect part, and determined by the relationship,

$$R_2^2 - R_3 = 0, \quad (7)$$

which is equivalent to the case when no Poisson noise is added after the rebinning. Thus,

$$t_{2max} = t_0 R_2^2. \quad (8)$$

This  $t_{2max}$  can be also used as a rough estimate of the effective image depth. The  $t_{2max}$  provides an estimate of the image depth much more effectively than the conventional simple exposure time because  $t_{2max}$  is related to a quantity that is affected both by exposure time and redshift, and thus enabling us to quantitatively compare exposure times of observations involving targets at different redshifts (e.g. 100 ksec at  $z=0.1$  and 100 ksec at  $z=0.9$ ).

Although we suspected that our ellipticity and position angle were quite robust, as a precaution we investigated the possible systematics on these measures introduced by various exposure times and redshifts, using our scaling technique described above.

In Fig. 1, we demonstrate our technique of simulating desired exposure time and redshift using the real optical image of the BCG at the cluster center taken with Subaru Suprime-Cam. Original and modified exposure time and redshift of an example cluster (Abell 2219) are shown with north up and east left, where (a) original image:  $\text{exptime}(t)=240\text{s}$ , and  $\text{redshift}(z)=0.228$ , (b) simulated shorter

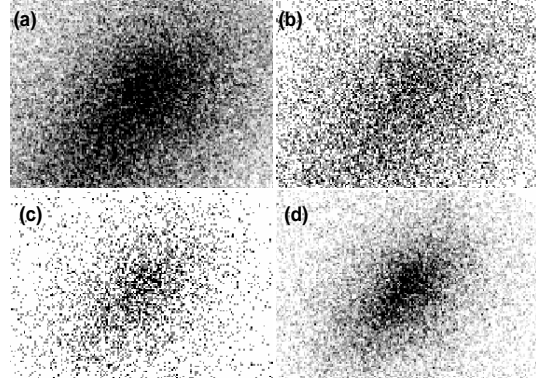


**Figure 2.** Similarly with Fig. 1, X-ray images from Chandra ACIS, of Abell 2219 are shown with original and modified exposure time and redshift. North is up and east is left. (a) Original:  $t=41\text{ks}$ ,  $z=0.228$  (b) Simulated shorter exposure:  $t=10\text{ks}$  ( $z=0.228$ ) (c) Simulated High- $z$  image:  $z=0.9$  ( $t=41\text{ks}$ ) (d) Prolonged exposure at High- $z$ :  $t=188\text{ks}$ ,  $z=0.9$ .

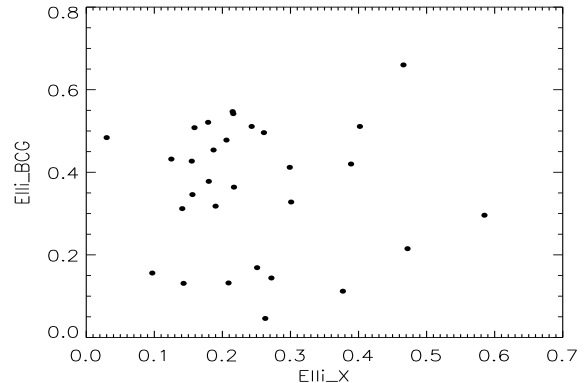


**Figure 3.** Ellipticity of BCGs is plotted against ellipticity of the X-ray morphology of the host clusters. Interestingly, no clear correlation is seen.

exposure image with  $t=10\text{s}$ , (c) simulated high- $z$  image with  $z=0.9$ ,  $t=240\text{s}$ , and (d) simulated prolonged exposure at high- $z$  with  $t=1092\text{s}$ ,  $z=0.9$ .

Similarly, in Fig. 2, we use the real X-ray images of Abell 2219 from Chandra ACIS, and simulated various exposures and redshifts, where (a) original image with  $t=41\text{ks}$ ,  $z=0.228$ , (b) simulated shorter exposure:  $t=10\text{ks}$  ( $z=0.228$ ), (c) simulated High- $z$  image:  $z=0.9$  ( $t=41\text{ks}$ ), and (d) prolonged exposure at High- $z$ :  $t=188\text{ks}$ ,  $z=0.9$ .

Using this technique, we simulated datasets with various exposure times and redshifts, and measured our cluster parameters. We found that our X-ray and optical position angles are robust against various exposure times and redshifts. Similarly, we found that other morphological measures such as, the ellipticity and asymmetry are quite robust, as well.

## 4.2 Analyses

Table 1 shows a summary of our optical cluster sample, where  $\Delta\text{PA}$  is an acute relative angle between the position angle of X-ray ( $\text{PA}_X$ ) and BCG ( $\text{PA}_{\text{BCG}}$ ), namely, the

**Table 1.** Summary of optical cluster sample

Cluster	z (redshift)	PA_X (degree)	PA_BCG (degree)	$\Delta PA^a$ (degree)	Elli_X	Elli_BCG
a2034	0.110	206.9	22.24	4.65	0.15	0.50
a2069	0.114	327.7	331.8	4.18	0.46	0.66
a750	0.163	249.0	249.6	0.66	0.14	0.31
rxj1720	0.164	355.3	32.08	36.7	0.15	0.34
a523	0.203	192.4	228.6	36.2	0.26	0.49
a963	0.206	175.9	347.0	8.85	0.15	0.42
a261	0.224	225.8	14.48	31.3	0.14	0.13
a2219	0.228	309.5	-79.5	29.0	0.38	0.42
a2390	0.233	298.6	-57.6	3.76	0.30	0.52
rxj2129	0.235	246.0	65.28	0.71	0.21	0.54
a2631	0.278	258.2	84.27	6.07	0.29	0.41
a1758	0.280	308.7	85.53	43.2	0.47	0.21
a2552	0.299	201.7	216.4	14.7	0.18	0.45
a1722	0.327	204.4	357.7	26.6	0.27	0.14
zwc13959	0.351	333.4	346.7	13.3	0.21	0.36
a370	0.357	187.2	86.96	79.7	0.37	0.11
rxj1532	0.361	227.7	78.24	30.5	0.18	0.37
zwc11953	0.373	351.2	306.3	44.8	0.24	0.51
zwc12661	0.382	159.5	206.9	47.3	0.12	0.43
zwc10024	0.390	5.200	246.6	61.4	0.03	0.48
rxj2228	0.412	263.7	56.27	27.4	0.21	0.54
rxj1347	0.451	359.2	343.8	15.3	0.20	0.13
ms0451	0.540	279.9	344.9	65.0	0.26	0.04
cl0016	0.541	228.7	244.6	15.9	0.19	0.31
ms2053	0.583	304.8	336.8	32.0	0.25	0.16
rxj1350	0.810	334.2	308.9	25.2	0.20	0.47
rxj1716	0.813	236.2	255.1	18.9	0.17	0.52
ms1054	0.830	266.1	35.96	50.1	0.40	0.51
rxj0152	0.835	221.6	231.0	9.46	0.58	0.29
wga1226	0.890	284.5	264.6	19.8	0.09	0.15

a:  $\Delta PA$  is an acute angle of  $PA_{BCG} - PA_X$

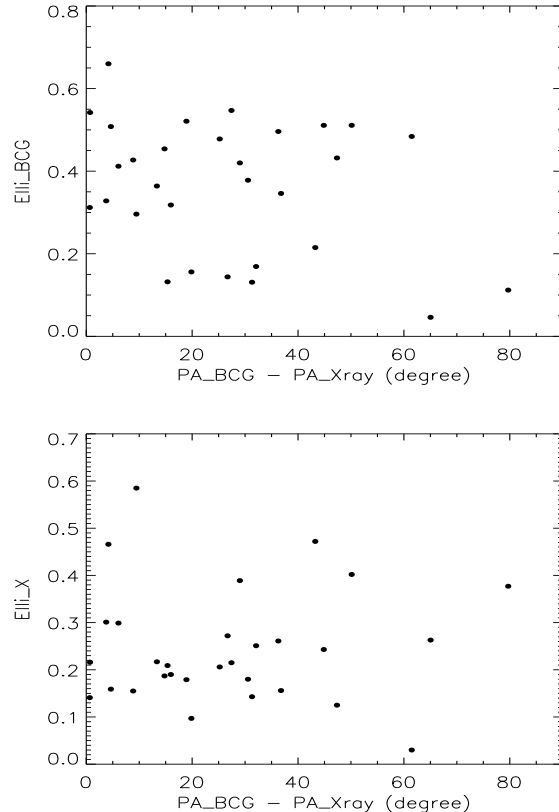
relative position angle differences greater than 90 degree are ‘folded’ and changed to be acute ranging between 0 and 90 degree. Despite the robust nature of our measures, we modify, as a precaution, all of the X-ray and optical observations to be equivalent to  $z=0.9$  and  $t=t_{max}$  to eliminate any possible small systematics, but otherwise to maximize the image quality.

In Fig. 3, the ellipticity of cluster X-ray morphology is plotted against the ellipticity of optical morphology of BCGs. Interestingly, in spite of expected alignment of two elliptical structures, there are a large scatter and we found no strong correlation in the relationship between the two ellipticities.

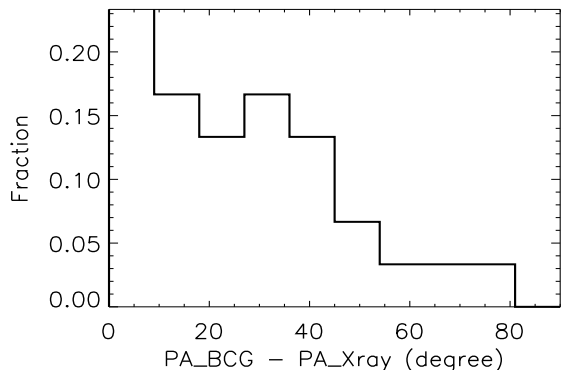
Fig. 4 shows the acute relative position angle difference between cluster X-ray morphology and BCG morphology plotted against the ellipticity of BCGs (top panel) and the ellipticity of cluster X-ray morphology (bottom panel). Fig. 4 shows that the position angle difference tends to be smaller than 45 degree, implying that BCGs tend to elongated in the same direction of the X-ray distribution of their host clusters, particularly for clusters exhibiting relatively high ellipticity in their optical BCG morphology and/or in their cluster X-ray morphology. Meanwhile, for clusters with very low BCG or X-ray ellipticity (ellipticity  $< 0.1$ ) position angle are generally poorly determined, and thus position angle difference can be inaccurate.

Fig. 5 shows the frequency distribution of the position angle difference. There is a strong tendency that we have more clusters with an angle difference less than 45 degrees, consistent with the observation made in Fig. 4.

To test this trend more rigorously, we first employed the Kolmogorov-Smirnov (K-S) test. The null hypothesis here is that our sample can be drawn from a parent population of random position angle differences. However, the K-S test detects the deviation from the parent population (here the population of random position angle differences), thus it may lose some sensitivity for testing the cluster alignment, where it is likely that position angle difference is systematically lower than the random sample. To increase



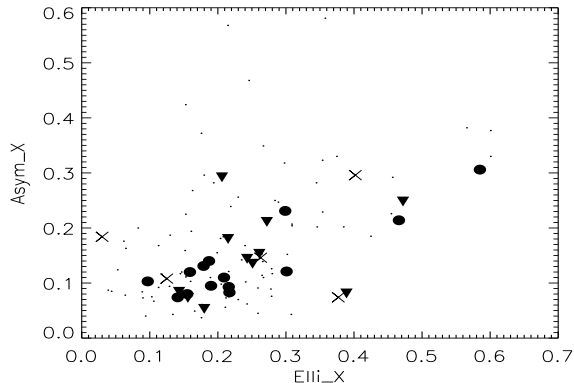
**Figure 4.** The acute position angle difference plotted versus ellipticity of BCGs (top panel) and ellipticity of cluster X-ray emission (bottom panel). The position angle difference is determined by the difference between the cluster X-ray position angle and the position angle of BCG galaxy. Figures illustrate that clusters with the position angle difference less than 45 degree tend to be more abundant, particularly for high ellipticity BCGs or clusters, implying that cluster X-ray emission and optical light from BCG are aligned.



**Figure 5.** The frequency distribution of the position angle difference. There is a tendency that we have more clusters with an angle difference less than 45 degrees, consistent with the observation made in Fig. 4 implying that cluster X-ray emission and optical light from BCG are aligned.

**Table 2.** Significance levels of the alignment for various luminous galaxies

Statistics	BCG	LG2	LG3	LG4	LG5
K-S	99.93	81.67	49.93	4.22	8.99
Rank Sum	99.99	83.06	57.09	54.51	63.33

**Figure 6.** X-ray morphology versus BCG alignment: Cluster X-ray asymmetry is plotted against cluster X-ray ellipticity. Large solid circles are clusters showing strong alignment with BCG-to-cluster position angle difference less than 20 degree, while solid triangles are clusters showing the “modest” alignment, but with position angle difference between 20 and 45 degree. Crosses represent clusters with no sign of the alignment, and small dots are clusters in our main sample without optical Subaru data. No clear trends are visible regarding frequency or degree of the alignment with respect to X-ray morphology, which can be interpreted as lack of dependence on the dynamical status of clusters.

the sensitivity to an alignment signal, as a second test we employed the Wilcoxon-Mann-Whitney rank-sum test. The null hypothesis of this test is that the position angle difference is not systematically smaller or larger than the random sample. Therefore the test is insensitive to an excess of angles around the mean (i.e. 45 deg). When applied to our sample, both K-S and rank-sum tests show, not surprisingly the strong alignment signals, and we find that the null hypothesis can be rejected with 99.93% and 99.99% confidence, respectively, thus confirming that BCGs are significantly aligned to the X-ray emissions of the host clusters. We have also investigated the alignment of other luminous non-BCG galaxies to the X-ray emissions and we found no significant alignment. The results are summarized in table 2, where LG2 is the second brightest galaxy, LG3 is the third brightest galaxy, and LGn is the n-th brightest galaxy within a projected distance of 1 Mpc from the X-ray center.

In Fig. 6, we investigated possible dependence of the position angle alignment on the X-ray morphology of the clusters. In Fig. 6, the cluster X-ray asymmetry is plotted against cluster X-ray ellipticity. Large solid circles are clusters showing strong alignment between the cluster and BCG with position angle difference less than 20 degree, while solid triangles are clusters showing the alignment, but with position angle difference between 20 and 45 degree. Crosses represent clusters with no sign of the alignment, and small dots

are clusters in our main X-ray sample without optical Subaru data. No clear trends are evident regarding frequency or degree of the alignment with respect to X-ray morphology.

We have also attempted to investigate possible dependence of the alignment on cluster redshifts. We found that for clusters less than  $z=0.35$ , both K-S and rank-sum tests show that the null hypothesis can be rejected with 99.92% and 99.99% confidence, respectively, while for clusters greater than or equal to  $z=0.35$ , alignment signals are somewhat weaker that the null hypothesis can be rejected with 93.88% and 83.69% confidence, respectively for K-S and rank-sum tests. Similarly, we have investigated the dependence of the alignment on the cluster X-ray bolometric luminosity ( $L_{bol}$ ), and we did not find any significant trend: for clusters with  $L_{bol}$  greater than or equal to  $2 \times 10^{45}$  erg/s, the null hypothesis can be rejected with 93.45% and 96.42% confidence, while for clusters with  $L_{bol}$  smaller than  $2 \times 10^{45}$  erg/s, the null hypothesis can be rejected with 99.78% and 99.90% confidence, respectively for K-S and rank-sum tests.

## 5 SUMMARY

We investigated the influence of environment on cluster galaxies by examining the alignment of the BCG position angle with respect to the host cluster X-ray position angle. The cluster position angles were measured using high spatial resolution X-ray data taken from the Chandra ACIS archive, that significantly improved the determination of the cluster shape compared to the conventional method of using optical images. Meanwhile, those of the BCGs were measured using high spatial resolution optical images taken with Suprime-Cam mounted on Subaru 8m telescope.

We found a strong indication of an alignment between the cluster X-ray emission and optical light from BCGs, while we see no clear direct correlation between the ellipticity of X-ray morphology and optical BCG morphology despite of the apparent alignment of two elliptical structures. In the hierarchical structure formation models, the alignment effect could be produced by clustering models of structure formation such as the cold dark matter model (e.g. Salvador-Sole & Solanes 1993; West 1994; Usami & Fujimoto 1997; Onuora & Thomas 2000; Faltenbacher et al. 2002, 2005). The existence of the alignment effects is also consistent with a cosmic structure formation model such as the hot dark matter model (e.g. Zeldovich 1970), where clusters and galaxies form by fragmentation in already flattened sheet- and filament-like structures.

We have also investigated possible dependence of the position angle alignment on the X-ray morphology of the clusters, and no clear trends are found. If the X-ray morphology of clusters reflects dynamical status of clusters (e.g. Hashimoto et al. 2004), the fact that no trends are evident regarding frequency or degree of the alignment with respect to X-ray morphology may be consistent with an interpretation as a lack of dependence of alignment on the dynamical status of clusters. Primordial galaxy alignments in clusters can be damped by various mechanisms such as the exchange of angular momentum in galaxy encounters, violent relaxation, and secondary infall (e.g. Quinn & Binney 1992; Coutts 1996) over a Hubble time. Thus, in highly relaxed clusters, we might naively expect to observe weaker primor-

dial galaxy alignment, because there has been sufficient time to mix the phases. The fact that we do not see any significant alignment trend with respect to the X-ray morphology may provide an important constrain on these damping scenarios.

## ACKNOWLEDGMENTS

This work is based in part on data collected at Subaru Telescope and obtained from the SMOKA, which is operated by the Astronomy Data Center, National Astronomical Observatory of Japan. We thank our referee, Dr. Michael West for his comments, which improved the manuscript. YH thanks Hiromi Hashimoto for the help retrieving the data from SMOKA.

## REFERENCES

- Binggeli B., 1982, *A&A*, 107, 338  
 Carter D., Metcalfe N., 1980, *MNRAS*, 191, 325  
 Chambers S., Melott A., Miller C., 2000, *ApJ*, 544, 104  
 Chambers S., Melott A., Miller C., 2002, *ApJ*, 565, 849  
 Coutts A., 1996, *Monthly Notices of the Royal Astronomical Society*, 278, 87  
 Dressler A., 1978, *ApJ*, 226, 55  
 Ebeling H., Edge A., Allen S., Crawford C., Fabian A., Huchra J., 2000, *MNRAS*, 318, 333  
 Ebeling H., Edge A., Böhringer H., Allen S., Crawford C., Fabian A., Voges W., Huchra J., 1998, *MNRAS*, 301, 881  
 Faltenbacher A., Allgood B., Gottlobler S., Yepes G., Hoffman Y., 2005, *MNRAS*, 362, 1099  
 Faltenbacher A., Gottlobler S., Kerscher M., Muller V., 2002, *A&A*, 395, 1  
 Flin P., 1987, *MNRAS*, 228, 941  
 Fuller T., West M., Bridges T., 1999, *ApJ*, 519, 22  
 Gioia I., Maccacaro T., Schild R., Wolter A., Stocke J., Morris S., Henry J., 1990, *ApJS*, 72, 567  
 Hashimoto Y., Barcons X., Böhringer H., Fabian A., Hasinger G., Mainieri V., Brunner H., 2004, *A&A*, 417, 819  
 Hashimoto Y., Böhringer H., Henry J., Hasinger G., Szokoly G., 2007b, *A&A*, 467, 485  
 Hashimoto Y., Henry J., Böhringer H., 2007a, *MNRAS*, 380, 835  
 Hashimoto Y., Oemler Jr A., Lin H., Tucker D., 1998, *ApJ*, 499, 589  
 Hasinger G., Giacconi R., Gunn J., Lehmann I., Schmidt M., Schneider D., Truemper J., Wambsganss J., Woods D., Zamorani G., 1998, *A&A*, 340, L27  
 Henry J., Gioia I., Maccacaro T., Morris S., Stocke J., Wolter A., 1992, *ApJ*, 386, 408  
 Henry J., Henriksen M., 1986, *ApJ*, 301, 689  
 Henry J., Mullis C., Voges W., Böhringer H., Briel U., Gioia I., Huchra J., 2006, *ApJS*, 162, 304  
 Landolt A., 1992, *AJ*, 104, 340  
 Miyazaki S., Sekiguchi M., Imi K., Okada N., Nakata F., Komiyama Y., 1998, *Proc. SPIE*, 3355, 363  
 Onuora L., Thomas P., 2000, *MNRAS*, 319, 614  
 Perlman E., Horner D., Jones L., Scharf C., Ebeling H., Wegner G., Malkan M., 2002, *ApJS*, 140, 265  
 Plionis M., 1994, *ApJS*, 95, 401  
 Plionis M., Basilakos S., 2002, *MNRAS*, 329, L47  
 Plionis M., Benoist C., Maurogordato S., Ferrari C., Basilakos S., 2003, *ApJ*, 594, 144  
 Porter A., Schneider D., Hoessel J., 1991, *AJ*, 101, 1561  
 Quinn T., Binney J., 1992, *Monthly Notices of the Royal Astronomical Society*, 255, 729  
 Rhee G., Katgert P., 1987, *A&A*, 183, 217  
 Rhee G., Latour H., 1991, *A&A*, 243, 38  
 Rosati P., Della Ceca R., Norman C., Giacconi R., 1998, *ApJ*, 492, L21  
 Salvador-Sole E., Solanes J., 1993, *ApJ*, 417, 427  
 Sarazin C., 1986, *RvMP*, 58, 1  
 Sastry G., 1968, *PASP*, 80, 252  
 Schindler S., Guzzo L., Ebeling H., Böhringer H., Chincarini G., Collins C., de Grandi S., Neumann D., Briel U., Shaver P., et al., 1995, *A&A*, 299, L9  
 Splinter R., Melott A., Linn A., Buck C., Tinker J., 1997, *ApJ*, 479, 632  
 Struble M., 1990, *AJ*, 99, 743  
 Ulmer M., McMillan S., Kowalski M., 1989, *ApJ*, 338, 711  
 Usami M., Fujimoto M., 1997, *ApJ*, 487, 489  
 van Haarlem M., van de Weygaert R., 1993, *ApJ*, 418, 544  
 Vikhlinin A., McNamara B., Forman W., Jones C., Quintana H., Hornstrup A., 1998, *ApJ*, 502, 558  
 West M., 1994, *MNRAS*, 268, 79  
 West M., Jones C., Forman W., 1995, *ApJ*, 451, L5  
 West M., Villumsen J., Dekel A., 1991, *ApJ*, 369, 287  
 Yagi M., Kashikawa N., Sekiguchi M., Doi M., Yasuda N., Shimasaku K., Okamura S., 2002, *AJ*, 123, 66  
 Zeldovich Y., 1970, *A&A*, 5, 168